

Investigation of Solidification and Precipitation Behavior of Si-Modified 7075 Aluminum Alloy Fabricated by Laser-Based Powder Bed Fusion



GUICHUAN LI, SURAJ DINKAR JADHAV, ARTURO MARTÍN, MARIA L. MONTERO-SISTIAGA, JEROEN SOETE, MARIA SAN SEBASTIAN, CARMEN M. CEPEDA-JIMÉNEZ, and KIM VANMEENSEL

Fabrication of high strength aluminum alloys using laser-based powder bed fusion (L-PBF) encounters challenges, including the occurrence of solidification cracks and the loss of volatile elements, such as Zn and Mg. The current work developed a Si-modified Al7075 alloy aiming at introducing eutectic phases to mitigate the solidification cracking during L-PBF. Based on Kou's model, the addition of Zn and Mg decreased the crack susceptibility from 6504 °C to 5966 °C, and the addition of 3.74 wt pct of Si further decreased the crack susceptibility to 3960 °C. The Al7075 alloy fabricated by L-PBF exhibited a large amount of solidification cracks extending throughout the sample. Crack-free samples with a relative density of 99.94 pct, as inspected by X-ray microcomputed tomography, were achieved for the developed Si-modified Al7075 alloy. The microstructure showed a transition from a coarse columnar microstructure to a refined mixed columnar + equiaxed microstructure after alloy modification, with a concomitant grain size reduction from 59.0 ± 42.2 to 15.0 ± 9.4 μm . Moreover, Si, Mg_2Si , and Al_2Cu phases were detected in the Si-modified Al7075 alloy. After a direct ageing heat treatment, the Si-modified Al7075 alloy showed minimal age hardening effect with a peak hardness of $(146 \pm 3 \text{ Hv})$.

<https://doi.org/10.1007/s11661-020-06073-9>

© The Minerals, Metals & Materials Society and ASM International 2020

I. INTRODUCTION

LASER-BASED powder bed fusion (L-PBF), also known as selective laser melting (SLM), is a powder-based additive manufacturing (AM) technique utilizing a laser as the energy source, allowing to manufacture complex-shaped metal components by additive consolidation of powder layers.^[1] Compared to conventional subtractive manufacturing processes, AM offers immanent advantages for medium-low batch production, owing to its capability to fabricate customized and complex-shaped parts as an integral piece without the need for expensive molds and tooling.^[2] Moreover, due to the steep thermal gradients and high

cooling rates during L-PBF, 3D-printed components exhibit enhanced mechanical performance. L-PBF processed metals owe their enhanced strength to the presence of supersaturated solid solutions and non-equilibrium phases, as well as to their refined solidification microstructures with high dislocation densities.^[3] The formation of a supersaturated matrix in L-PBF processed aluminum alloys offers opportunities to further improve the strength by precipitation during subsequent heat treatment. This is particularly interesting in the 2xxx, 6xxx, and 7xxx series aluminum alloys, as they obtain their mechanical strength from the precipitate formation during post-heat treatments.

High strength Al-Zn-Mg-Cu alloys, especially AA7075 aluminum alloys, are widely used for the fabrication of structural components in the automotive and aerospace industries due to their high specific strength and good fatigue properties.^[4,5] However, traditional cold deformation manufacturing techniques are unable to fabricate AA7075 aluminum alloy components with complicated geometries because of their poor formability and high elastic spring back.^[6] Due to its inherent layer-by-layer building fashion, L-PBF offers completely new opportunities to design and manufacture metallic structures and components with

GUICHUAN LI, SURAJ DINKAR JADHAV, MARIA L. MONTERO-SISTIAGA, JEROEN SOETE, and KIM VANMEENSEL are with the Department of Materials Engineering, KU Leuven, Kasteelpark Arenberg 44, 3001 Heverlee, Belgium. Contact e-mail: guichuan.li@kuleuven.be ARTURO MARTÍN and CARMEN M. CEPEDA-JIMÉNEZ are with the IMDEA Materials Institute, C/Eric Kandel, 2, 28906 Getafe, Madrid, Spain. MARIA SAN SEBASTIAN is with the IK4 LORTEK Technological Centre, Arranomendia 4A, 20240 Ordizia, Spain.

Manuscript submitted May 5, 2020; accepted October 17, 2020.

Article published online November 15, 2020

high complexity and precision.^[7] Unfortunately, the widespread application of L-PBF as a manufacturing technique to fabricate high strength Al-Zn-Mg-Cu alloys is hindered by solidification cracking, also known as hot tearing. A major contributor to this phenomenon is the large solidification interval, extended under rapid cooling conditions, that is characteristic for this type of alloys.^[8] The extensive vaporization of the main strengthening alloying elements, *i.e.*, Zn and Mg, as a result of their high equilibrium vapor pressure and low boiling point, during the L-PBF process, results in inferior mechanical properties.^[2,9] Thus, it is crucial to address these issues to enhance the performance and expand the applications of high strength aluminum utilizing the L-PBF technique.

Solidification cracking usually occurs during the last stage of solidification when the last fraction of liquid metal, retained as a liquid film within the inter-dendritic regions of solidified dendritic/columnar grains, cannot accommodate the tensile strain caused by the volumetric solidification shrinkage and thermal contraction.^[10,11] Materials with high susceptibility to solidification cracking often exhibit a broad solidification range, a relatively high coefficient of thermal expansion (CTE), a high viscosity of the interdendritic liquid, and a poor liquid backfilling ability.^[12,13] The steep thermal gradients and ultrahigh cooling rates (10^3 to 10^7 K/s)^[14,15] that are characteristic for L-PBF intensify the tensile stress/strain and strain rates applied on the liquid film during solidification, resulting in an even higher solidification cracking tendency. Many remedies have been proposed to mitigate the solidification cracking problem experienced by high strength aluminum alloys during laser-aided additive manufacturing and welding. Mertens *et al.*^[16] successfully applied base plate pre-heating up to 400 °C, decreasing the crack density and distortion by reducing the thermally induced residual stresses. However, baseplate pre-heating failed to eliminate the solidification cracks.^[17] Grain refinement by inoculation has proven to be one of the efficient approaches to mitigate solidification cracking. For example, the incorporation of TiB₂ particles in 2000^[18,19] and 6000^[20] series aluminum alloys, and the addition of TiC nanoparticles^[21] in the Al7075 alloy significantly refine the grains, resulting in crack-free components with fine equiaxed grain structure. The grain refinement effect is due to the good crystallographic coherency between the inoculants and the FCC Al matrix. The grain refinement efficiency of the particles and the mechanical properties of the particle-reinforced materials can degrade due to the oxidation of the inoculant particles and the formation of brittle matrix-reinforcement interfacial products. Besides, Martin *et al.*^[22] decorated Al powders with ZrH₂ nanoparticles to *in-situ* form Al₃Zr-L1₂ particles, acting as heterogeneous nucleation sites during solidification of the Al matrix phase. The formation of solidification cracks was avoided because the presence of equiaxed grains increasing the backfilling ability. When the liquid film was confined between equiaxed grains, it could better accommodate the thermal strain that developed at the end of solidification. However, the pronounced loss of alloying elements, *i.e.*, Zn and Mg,

and the presence of hydrogen pores in the parts generated by the decomposition of ZrH₂, resulted in reduced mechanical properties and reliability of the final components. Similar approaches, based on the addition of trace elements such as Zr and Sc, to mitigate solidification cracks have been reported.^[23–27] Moreover, alloy modification, aiming at improving the fluidity, has proven to be another approach to mitigate solidification cracking. Montero-Sistiaga *et al.*^[28] showed that mixing 4 wt pct of micrometer-sized pure Si powder and 96 wt pct of Al7075 powder successfully prevented the formation of solidification cracks by improving the fluidity of the molten material and refining the grains. However, the grain refinement mechanism by adding Si powders is not well understood. Si-containing filler materials have been widely used in laser welding as they improve the liquid fluidity and backfilling ability during the terminal stage of solidification. Furthermore, the addition of Si reduced the freezing range, due to the eutectic α -Al/Si formation.^[29]

Numerous criteria have been proposed to predict the solidification cracking susceptibility in the computer-aided material design of aluminum alloys. The solidification temperature range, determined by the liquidus and solidus temperatures, has been appreciated as a simple index to rank the solidification cracking susceptibility. The alloys with a broader solidification range are more susceptible to solidification cracking because the liquid film is more prone to be ruptured by a larger substantial strain and reduced backfilling ability.^[12] The first model with a physically sound basis, RDG model,^[30] was proposed by Rappaz, Drezet and Gremaud. They assumed that the cracking would occur when a critical strain rate is achieved by considering both shrinkage and uniaxial deformation. However, the grain boundary was not included yet. Kou^[31] proposed a more developed model considering three factors: (a) the tensile strain separating the grain boundary induced by solidification shrinkage and thermal contraction; (b) the bridging between two adjacent grains which resists cracking resulting from grain growth; and (c) the liquid feeding at the terminal stage of solidification. The steepness of the $T-f_s^{1/2}$ curve was derived as an index of cracking susceptibility, $\left|dT/d\left(f_s^{1/2}\right)\right|$, near $f_s^{1/2} = 1$, where T stands for temperature and f_s stands for the mass fraction of solid. The material with higher steepness shows higher cracking susceptibility. This model has been later experimentally validated for Al-Mg-Si, Al-Cu-Mg, and Al-Cu-Si alloy systems by Liu and Kou.^[32]

In this study, an Al-Zn-Mg-Cu-Si alloy was proposed to fabricate crack-free parts for the L-PBF process. Firstly, the influence of Zn, Mg, and Si addition on the solidification behavior of the Al7075 alloy under equilibrium and non-equilibrium conditions was investigated using computational thermodynamics. The effect of Zn + Mg addition and Si additions on the cracking susceptibility of the Si-modified Al7075 alloy was evaluated based on the maximum steepness $\left|dT/d\left(f_s^{1/2}\right)\right|$, which was proposed by Kou. Secondly,

Differential Scanning Calorimetry (DSC) and L-PBF experiments, which represent equilibrium and non-equilibrium solidification conditions, respectively, were performed to verify the predictions. The influence of the addition of alloying elements on the solidification behavior was discussed to clarify why solidification cracking did not occur in the new alloy. Finally, the influence of Si addition, combined with a modified alloy composition that compensated for the Zn and Mg losses during L-PBF, on the hardness after post-heat treatment was investigated. The current study provides new insights into the development of crack-free high strength aluminum alloys for AM.

II. MATERIALS AND EXPERIMENTAL METHODS

A. Powder Production and Characterization

Commercial Al7075 alloy powder supplied by LPW technology Ltd. (UK) was used for the preliminary test as a reference. A Si-modified Al7075 alloy with adjusted Zn and Mg content was designed to introduce additional eutectic phases and compensate for the Zn and Mg loss based on the preliminary L-PBF test. The Si-modified Al7075 pre-alloy was produced at IMDEA Materials Institute (Spain) and the powder was obtained by gas atomization at CENIM-CSIC (Spain). Firstly, pre-alloys with the targeted composition were obtained by melting commercial pure Mg, Zn, Si and Al7075-T651 sheet provided by Alu-Stock S.A. (Spain). Secondly, Si-modified Al7075 alloy powders were produced in a LEIBOLD Gas Atomizer (model VIGA 2S) under argon atmosphere. The chemical composition of the starting powders, as measured by inductively coupled plasma-optical emission spectrometry (ICP-OES), is listed in Table I. Most powder particles exhibit a near-spherical shape with little internal pores. The particle size distribution was measured by a Beckman Coulter LS 13 320 laser diffraction particle size analyzer. The average particle diameter was 44.3 μm , with D10, D50 and D90 values of 17.8, 43.8, and 71.3 μm , respectively. The dynamic angle of repose measurements of the gas atomized Al-Zn-Mg-Cu-Si alloy powder show small angles of 27.9 and 30.9 deg for the average and avalanche angle, respectively, indicating a good flowability which is suitable for L-PBF. The powder characteristics, including morphology, particle size distribution and flowability, are summarized in Supplementary

Figure S-1. The theoretical density of the gas atomized powder was analyzed by gas pycnometry (Quantachrome MVP-6DC) using Helium gas. A jolting volumeter was used to determine the tap density. Four measurements were repeated to obtain the average theoretical and tap density. The tap density and theoretical density of the powder are 1.77 and 2.82 g/cm^3 , respectively, resulting in a tap to theoretical density ratio of 62.9 pct.

B. Laser Powder Bed Fusion Process and Heat Treatment

The L-PBF experiments were carried out on an in-house developed machine equipped with a 1 kW fiber laser. Cube-shaped samples with dimensions of $10 \times 10 \times 6 \text{ mm}^3$ were produced for processing parameter optimization and microstructural characterization. The samples were fabricated using different laser powers (250 to 350 W), scanning speeds (1000 to 1750 mm/s) and hatching spacing (70 to 105 μm). The layer thickness was fixed at 30 μm . The linear energy density (LED) defined as:

$$\text{LED (J/m)} = \frac{\text{Laser power, } P(\text{W})}{\text{Scanning speed, } v(\text{m/s})} \quad [1]$$

was used to describe the energy input from the laser source to the powder bed during processing. A bidirectional scanning strategy with 90 deg rotation between successive layers was applied. The building chamber was flushed with argon to minimize oxidation during the L-PBF process. The relative density of L-PBF-fabricated specimens versus linear energy density with three hatch spacing and corresponding OM images is shown in Supplementary Figure S-2. Dense cube-shaped specimens with a relative density exceeding 99.1 pct were fabricated at a linear energy density of 280.0 J/m (laser power 350 W, scan speed 1250 mm/s) using all the three hatch spacing, namely, 70, 90, and 105 μm . Image analysis shows that the highest relative density of 99.3 ± 0.1 pct is achieved using a laser power of 350 W, a scan speed of 1250 mm/s, a hatch spacing of 105 μm , and a layer thickness 30 μm , which is defined as the optimized parameter set in this study. The chemical compositions of as-built samples are listed in Table I. The Zn and Mg losses during the L-PBF process are 16.8 and 12.9 wt pct for the Al7075 alloy and 22.0 and 14.4 wt pct for the Si-modified Al7075 alloy, respectively. As-fabricated samples with optimized processing parameters were

Table I. Chemical Composition of Starting Powders and As-Built Samples of Al7075 and Si-Modified Al7075 Alloy Measured by ICP-OES

Alloy Composition (Wt Pct)	Al	Zn	Mg	Cu	Si	Cr	Fe
Al7075 Powder	bal.	4.82	1.94	1.52	0.22	0.18	0.14
Al7075 As-Built*	bal.	4.01	1.69	1.51	0.17	0.18	0.17
Si-Modified Al7075 Powder	bal.	6.54	3.12	1.52	3.85	0.19	0.08
Si-Modified Al7075 As-Built*	bal.	5.10	2.67	1.55	3.74	0.21	0.07

*The as-built samples were manufactured using the following combination of scan parameters: laser power 350 W, scanning speed 1250 mm/s, layer thickness 30 μm , and hatch spacing 105 μm .

subjected to direct ageing (DA) treatments at 120 °C and 150 °C for different holding times followed by air cooling. Ageing treatments were carried out in argon atmosphere using a vertical tube furnace.

C. Thermodynamic Simulations

Thermodynamic simulations were carried out to investigate the solidification and precipitation behavior of the Al7075 and Si-modified Al7075 alloys under equilibrium and non-equilibrium conditions using the TCAL6: Al-Alloys v6.0 database of the Thermo-Calc 2020-a software package. The chemical compositions in wt pct of as-built parts, given in Table I, were used for the simulations, specifically, Al-4.01Zn-1.69Mg-1.51-Cu-0.17Si for the Al7075 alloy and Al-5.10Zn-2.67Mg-1.55Cu-3.74Si for the Si-modified Al7075 alloy. Additionally, Al-5.10Zn-2.67Mg-1.55Cu alloy was calculated to evaluate the effect of Zn and Mg addition on the crack susceptibility. Al alloys with an overall composition of Al-5.10Zn-2.67Mg-1.55Cu with Si additions ranging from 0.17-8 (wt pct) were used to calculate and evaluate the effect of Si. Under equilibrium conditions, diffusion in both solid and liquid is assumed, while the diffusion in the liquid is infinitely fast compared to that in the solid phase and local equilibrium is only present at the solid/liquid interface when the Scheil-Gulliver solidification model is applied.^[33,34]

Moreover, $T-f_s^{1/2}$ curves adopted from the Scheil-Gulliver solidification model were plotted. The maximum steepness of the $T-f_s^{1/2}$ curve was calculated using the statistical slope function on three sets of $T-f_s^{1/2}$ values.

D. Materials Characterization

Image analysis was performed on cross-sectioned micrographs to determine the porosity content. At least four images covering an area of $2.7 \times 2.0 \text{ mm}^2$ were analyzed for each sample using Image J software. In addition, X-ray microcomputed tomography (μ -CT) was used to inspect internal pores and cracks in the as-built samples. A TeScan Unitom XL, equipped with a 230 kV/300 W microfocus X-ray tube and a 2856×2856 pixel detector, with a $150 \mu\text{m}$ pixel pitch was used. Scan voltage and power were set to 180 kV and 15 W respectively. A 1 mm thick aluminum filter was installed during the scans to reduce the intensity of low-energy X-ray photons. Cuboid samples ($4.5 \times 4.5 \times 5 \text{ mm}^3$) were scanned using a 360 deg rotation sector, with a 0.15 deg rotation step. The exposure timing was set to 200 ms. All the sectional planes were reconstructed in the TeScan Aquila reconstruction software. 3D renderings and analyses of the models, with an isotropic voxel size of $3 \times 3 \times 3 \mu\text{m}^3$, were generated in Avizo 2020.2. An Axioskop 40 A Pol optical microscope (OM) and an FEI Nova NanoSEM 450 scanning electron microscope (SEM) were used to characterize the microstructure. An acceleration voltage of 15 kV, spot size of 4 and working distance of 5 mm, were applied. The solidification and precipitation behavior were investigated based on Differential Scanning Calorimetry

(DSC) measurements, which were performed in a TA 2920 Scanning Calorimeter (TA Instruments) between 25 °C and 700 °C with a 5 °C/min heating and cooling rate. Crystallographic phases were analyzed by X-ray diffraction (XRD) using a Bruker D2 Phaser diffractometer using Cu-K α radiation. A step size of 0.02 deg and a scanning speed of 2 deg/min were selected for the measurements. The crystallographic orientation and grain size were characterized using electron backscattered diffraction (EBSD) which was carried out on an FEI Nova NanoSEM 450 microscope equipped with a TSL system. An acceleration voltage of 20 kV, a spot size of 5 and a step size of $1 \mu\text{m}$ were used for EBSD mapping. Hardness tests were performed in a Future Tech-700 Vickers hardness tester with a 0.5 kg load and 15 s indentation time. 7 points in the center of the cuboid sample at a height of around 2.5 mm were measured to calculate the average hardness.

III. RESULTS

A. Thermodynamic Simulations and Crack Susceptibility Prediction

Solidification sequence, phase constitution, and solidification microstructure are closely associated to the solidification conditions. Therefore, the non-equilibrium solidification behavior during L-PBF is expected to be different from the equilibrium solidification behavior experienced during a slow cooling process. In this section, equilibrium and non-equilibrium simulations are performed to predict the solidification behaviors during a slow, inside a calorimeter during DSC, and fast, during L-PBF, cooling process. Furthermore, the equilibrium solidification is used to predict the phase constitution after performing an ageing heat treatment on as-built parts.

1. Equilibrium Solidification

Figure 1 compares the solidification trajectories of the Al7075 and Si-modified Al7075 alloy under equilibrium conditions. The mass fraction of the various phases that form under equilibrium conditions is plotted as a function of temperature. As seen in Figures 1(a) and (b), the 7075 aluminum alloy, which is susceptible to solidification cracking during L-PBF, solidifies over a wide temperature range. The Al-FCC phase is expected to form at 630 °C, and its fraction increases continuously until the last liquid solidifies at 533 °C. As such, the solidification temperature range of the Al7075 alloy is defined as ~ 97 °C (630 °C-533 °C). As shown in Figures 1(c) and (d), the predicted liquidus temperature decreases by 20 °C from 630 °C to 610 °C for the Si-modified Al7075 alloy, while the solidus temperature decreases from 533 °C to 516 °C, resulting in a similar solidification range of ~ 94 °C (610 °C to 516 °C). Due to the presence of 0.17 wt pct Si as impurities in the Al7075 alloy, Mg_2Si phase is formed at the last stage of solidification. In addition, the Si phase and an increased amount of Mg_2Si phase are formed in the Si-modified

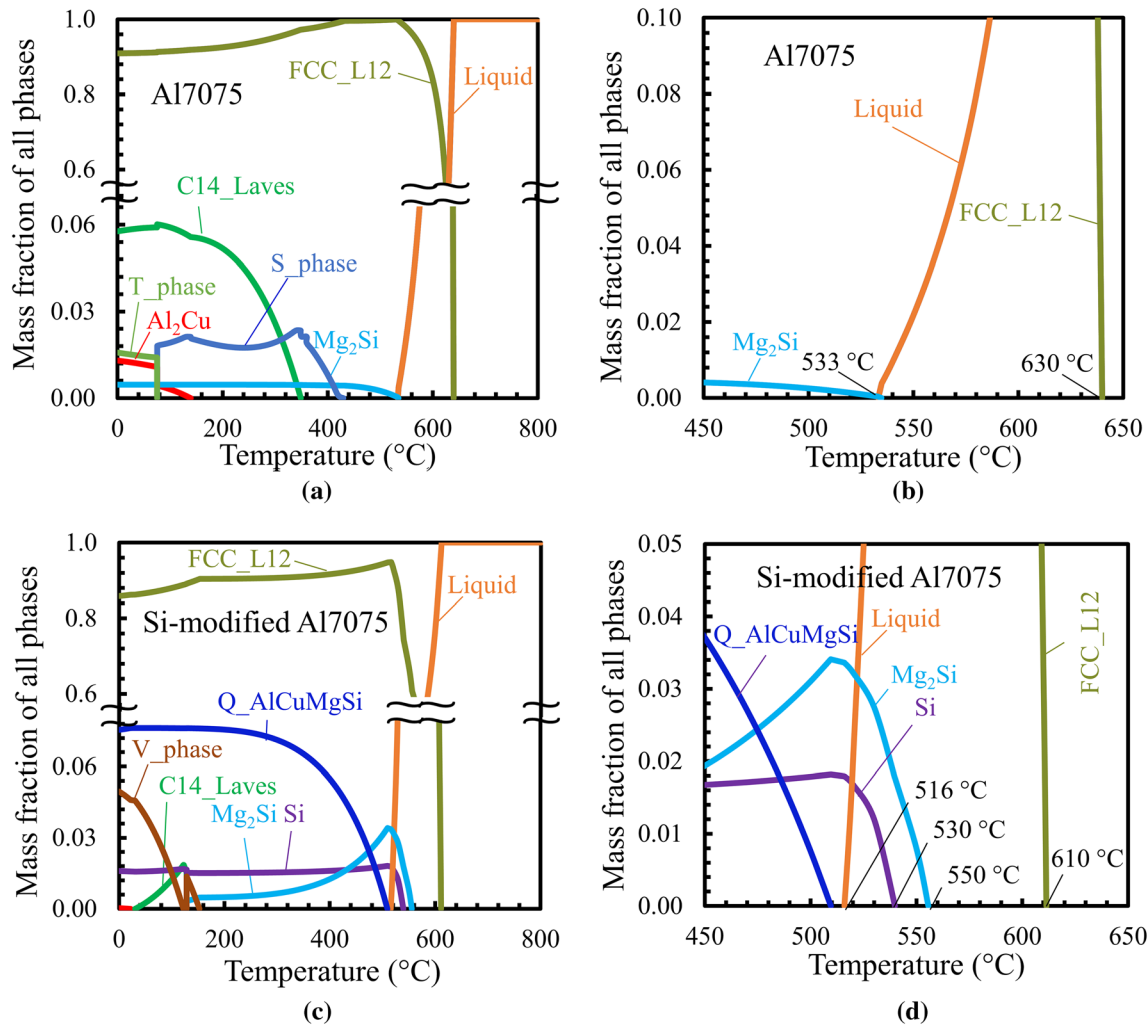


Fig. 1—The calculated solidification trajectories under equilibrium conditions: (a, b) Al7075 alloy and (c, d) Si-modified Al7075 alloy.

Al7075 alloy during the last stages of solidification at 550 °C and 530 °C, respectively.

Furthermore, the additions of Zn, Mg, and Si also impact on the solid-state phase transformations. In the unmodified Al7075 alloy, the S-phase (Al_2CuMg), C14_Laves phase (MgZn_2), and Al_2Cu phase form subsequently with the temperature decreasing to 432, 349, and 139 °C, respectively. It is noticed that the T-phase, which described as $\text{Mg}_{26}(\text{Al}, \text{Mg})_6(\text{Al}, \text{Zn}, \text{Cu}, \text{Mg})_{48}(\text{Al})_1$, consumes the S-phase at 75 °C during cooling. Thus, the room-temperature phases of the solidified 7075 alloy are the FCC Al matrix phase, T-phase, Al_2Cu , Mg_2Si , and the C14_Laves (MgZn_2) phase. After adding Zn, Mg, and Si, a Q-phase ($\text{Al}_5\text{Cu}_2\text{Mg}_8\text{Si}_6$) is formed instead of the S and T phase at 510 °C, followed by the precipitation of the V-phase with a described composition of $(\text{Al}, \text{Zn})_5(\text{Zn}, \text{Cu})_6(\text{Mg})_2$ at the expense of the Mg_2Si and the C14_Laves phase (MgZn_2). Thus, the room temperature phases of the Si-modified Al7075 alloy consist of Al-FCC, Q-phase, V-phase, and Si phase. Therefore, the addition of alloying elements not only modifies the

solidification behavior but also changes the nature of the secondary phases, which would result in different precipitation behavior during post heat treatment and concomitant altered mechanical performance.

2. Non-equilibrium (Scheil-Gulliver) solidification

Owing to the rapid solidification experienced by the alloys during the L-PBF process, a Scheil-Gulliver model was used to describe their non-equilibrium solidification behavior. The thermodynamically predicted solidification trajectories of the Al7075 and Si-modified Al7075 alloys under Scheil-Gulliver condition are shown in Figure 2(a). It is observed that the Si, Q-phase, Al_2Cu and Zn phase are formed in the Si-modified Al7075 alloy instead of the S, T and V-phase in the Al7075, and the formation of the MgZn_2 phase is not favored. Additionally, in contrast to equilibrium solidification, the solidification range is expanded from ~190 °C (640 °C to 450 °C) for the virgin Al7075 alloy to ~281 °C (611 °C to 330 °C) for the Si-modified Al7075 alloy under Scheil-Gulliver solidification conditions.

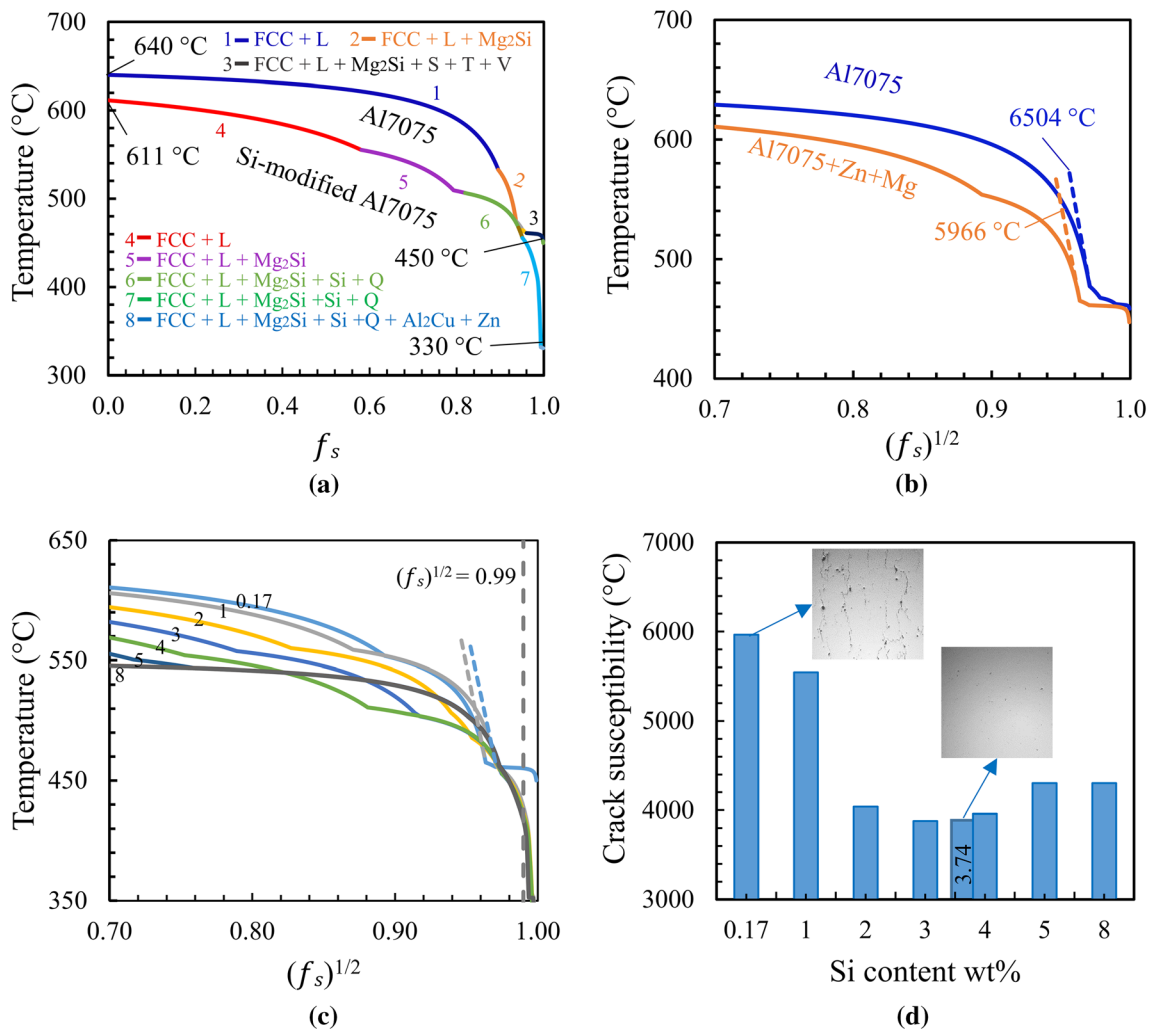


Fig. 2—(a) Computationally calculated solidification trajectories of Al7075 and Si-modified Al7075 alloy under non-equilibrium condition. (b) The T - $f_s^{1/2}$ curves showing the effect of Zn and Mg addition on the crack susceptibility, where T is the temperature and f_s is the mass fraction of solid. The maximum steepness of the curves is plotted as dashed lines. (c) T - $f_s^{1/2}$ curves of the Al-5.10Zn-2.67Mg-1.55Cu alloys with 0.17 to 8 wt pct Si additions, the dashed vertical line indicates $f_s^{1/2} = 0.99$. (d) Variation of crack susceptibility of Al-5.10Zn-2.67Mg-1.55Cu alloys as function of Si additions.

Furthermore, based on Kou's model, the maximum steepness $\left|dT/d(f_s^{1/2})\right|$ of the T vs $(f_s)^{1/2}$ curves is used as the solidification crack susceptibility index. If the maximum steepness occurs beyond $(f_s)^{1/2} = 0.99$, the steepness at $(f_s)^{1/2} = 0.99$ is regarded as the crack susceptibility index, as liquid film rupture does not take place at the very end of the solidification trajectory due to extensive bridging between grains. The effect of Zn and Mg additions as well as the Si contents on the crack susceptibility are evaluated separately. As shown in Figure 2(b), the addition of Zn and Mg slightly reduces the maximum steepness $\left|dT/d(f_s^{1/2})\right|$, i.e., the crack susceptibility, of the Al7075 alloy from around 6504 °C to 5966 °C. Figures 2(c) and (d) indicate that, as the Si content in the Al7075 alloy increases from 0.17 to 8

wt pct, the crack susceptibility initially decreases when Si content increased to 2 wt pct. In the Si range of 3 to 4 wt pct, the crack susceptibility reaches the lowest level and does not change significantly with increasing Si content. Subsequently, the crack susceptibility slightly increases again at a Si content of 5 wt pct and remains stable up to a Si content of 8 wt pct. The initial decrease in crack susceptibility is attributed to the change in phase constitution from S and T phases into Al₂Cu, C15_Laves phases, defined as (AlZnMgCuSi)₂(AlZnMgCuSi)₁, and Q phase. The increase of the crack susceptibility at 5 wt pct Si results from the formation of pure Si instead of the C15_Laves. Therefore, a Si content of 3 to 4 wt pct is suggested to achieve a low crack susceptibility, thus the ability to be processed by L-PBF. A crack susceptibility of 3960 °C is achieved by the Si-modified Al7075 alloy with 3.74 wt pct Si.

B. Equilibrium solidification behavior based on DSC measurements

DSC measurements of the Al7075 and the Si-modified Al7075 alloy were performed at a cooling rate of 5 °C/min to verify the predicted equilibrium solidification behavior. As shown in Figure 3(a), the addition of alloying elements lowers the liquidus temperature of the Al7075 alloy by 28 °C from 627 °C to 599 °C, which is consistent with the thermodynamic simulations shown in Figure 1. Additionally, three exothermic peaks appear in the DSC curve of the Si-modified Al7075 alloy at 599 °C, 557 °C, and 527 °C, respectively, contrary to the presence of a single exothermic Al-FCC peak in the Al7075 alloy. Their presence confirms that adding Si in the Al7075 alloy introduces two additional eutectic phases, namely Mg₂Si and Si. The Mg₂Si peak is not observed in the Al7075 alloy probably due to the low Si content.

Moreover, the effects of alloy modification on the solid-state phase transformation during cooling are observed in Figure 3b. The Al7075 alloy shows two exothermic peaks in the temperature range of 100 to 500 °C. The peak 2 which occurs at 465 °C is corresponding

to the precipitation of S-phase and the broad exothermic peak 1 at 176 °C results from the continuous precipitation of T-phase, Laves phase (MgZn₂), and Al₂Cu phase. Similar results have been reported by other researchers.^[28,35] In the Si-modified Al7075 alloy, two exothermic peaks occur at different temperature ranges compared to the Al7075 alloy. The peak 2 occurs at around 475 °C related to the precipitation of Q-phase as per the thermodynamic simulations. Additionally, the exothermic peak 1 that appears at 360 °C might arise from the formation of V-phase (Al-Zn-Cu-Mg). However, the temperature is higher than the predicted formation temperature of 180 °C.

Figures 3(c) and (d) depict the microstructure of the Si-modified Al7075 sample after melting at 700 °C and solidifying at a low cooling rate of 5 °C/min. The presence of the Mg₂Si, Si, Q-phase (Al-Cu-Mg-Si) and the V-phase (Al-Zn-Cu-Mg) is confirmed. Besides, the Al-Cr-Fe-Si intermetallic phase is also observed due to the presence of Fe and Cr impurities. No Laves phase (MgZn₂) could be traced during the microstructure analysis, which is consistent with the DSC measurements.

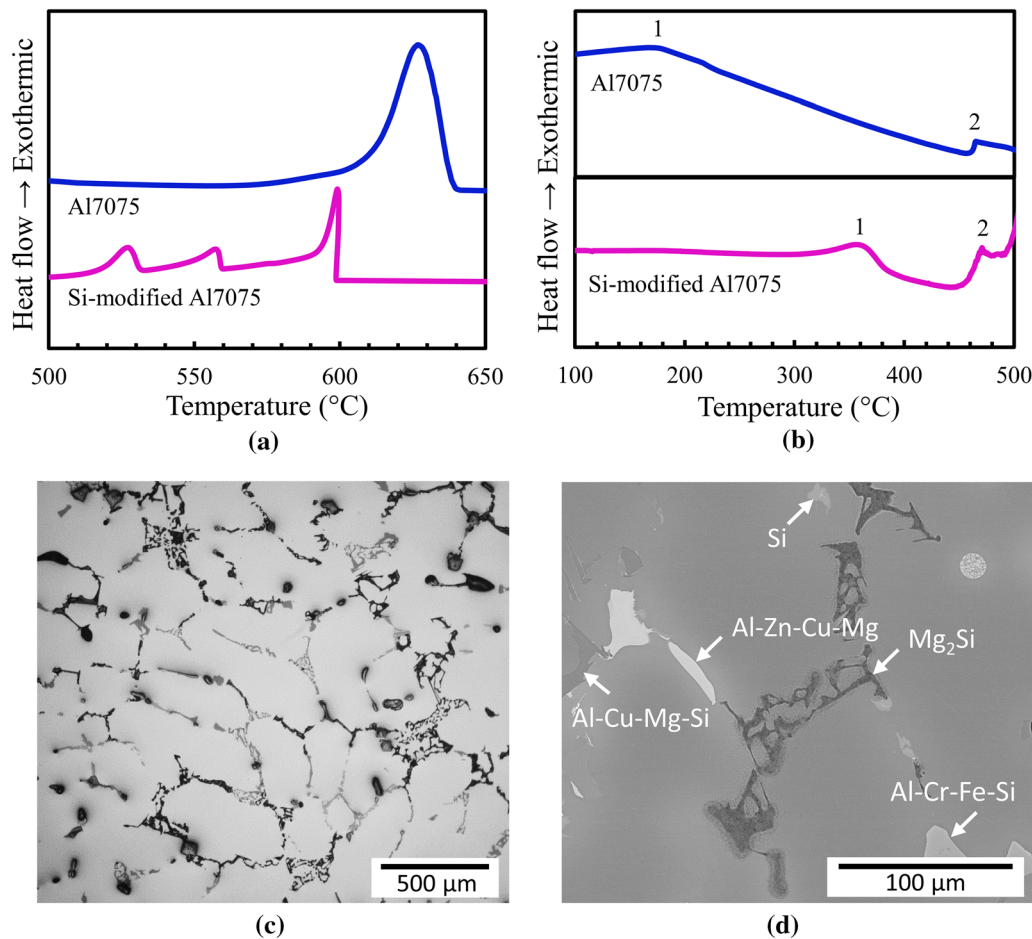


Fig. 3—DSC cooling curves of the Al7075 alloy and Si-modified Al7075 alloy in the temperature range of (a) 500 °C to 650 °C, (b) 100 °C to 500 °C, and (c, d) the microstructure of slowly solidified Si-modified Al7075 alloy obtained from the DSC measurement, applying a cooling rate of 5 °C/min.

C. Non-equilibrium Solidification During L-PBF Process

1. Inspection of defects

Laser scan parameters have been optimized to achieve dense samples during the L-PBF process. Relative density values determined using image analysis, as shown in Figure S-2, indicate that the highest relative density of 99.3 ± 0.1 pct is achieved in the Si-modified Al7075 alloy using the optimized scan parameter set of laser power 350 W, scan speed 1250 mm/s, hatch spacing $105 \mu\text{m}$, and layer thickness $30 \mu\text{m}$. Figure 4 compares the presence of cracks and internal porosities, as determined by X-ray microcomputed tomography ($\mu\text{-CT}$), between as-built Al7075 and Si-modified Al7075 samples, both manufactured using the optimized scan parameter set. The Al7075 sample shows a significantly higher amount of internal pores ~ 2.81 vol pct as compared to the Si-modified Al7075 alloy ~ 0.06 vol pct. A closer look at the pore morphology in the representative cuboids, as shown in Figure 4(a), shows a large amount of interconnected pores, which are solidification cracks, extending throughout the Al7075 samples. The cross-sections in Figure 4(b) indicate that the cracks are mainly parallel to the building direction (BD). As seen in Figures 4(c) and (d), crack-free Si-modified Al7075 samples with a small amount of pores are achieved by L-PBF. The remaining spherical pores are assumed to be hydrogen pores or gas pores due to the evaporation of Zn and Mg during the L-PBF process.^[36] It can be noticed that the relative density value of ~ 99.94 pct, as

obtained by X-ray $\mu\text{-CT}$, is slightly higher than ~ 99.3 pct, as obtained from image analysis. This is because pores smaller than $3 \times 3 \times 3 \mu\text{m}^3$ are below the detection limit of the X-ray $\mu\text{-CT}$ equipment and the less representative of 2-dimensional image analysis. However, these small pores are reported not to have significant influence on the static mechanical properties.^[37,38]

2. Microstructure

Representative micrographs of the Al7075 alloy and the Si-modified Al7075 alloy processed by the L-PBF technique are shown in Figure 5. The etched cross-sectional OM micrograph, shown in Figure 5(a), reveals the layer-wise microstructural features of the as-built sample consisting of alternating layers of hemispherical melt pools and continuous melt pools, a representative for the applied bi-directional scanning strategy with 90 deg rotation between consecutive layers. High magnification side-view SEM images of the as-built sample are presented in Figures 5b through d. The melt pools are identifiable due to the different solidification morphologies at different locations within the melt pool. In the melt pool center, mainly fine columnar dendritic cells that grow from the melt pool boundary towards the melt pool center are observed, while equiaxed dendritic cells are formed at the melt pool boundary. In contrast to the coarse dendritic solidification microstructure that was observed in the as-cast sample at a low cooling rate, as shown in Figure 3, the rapid solidified Si-modified

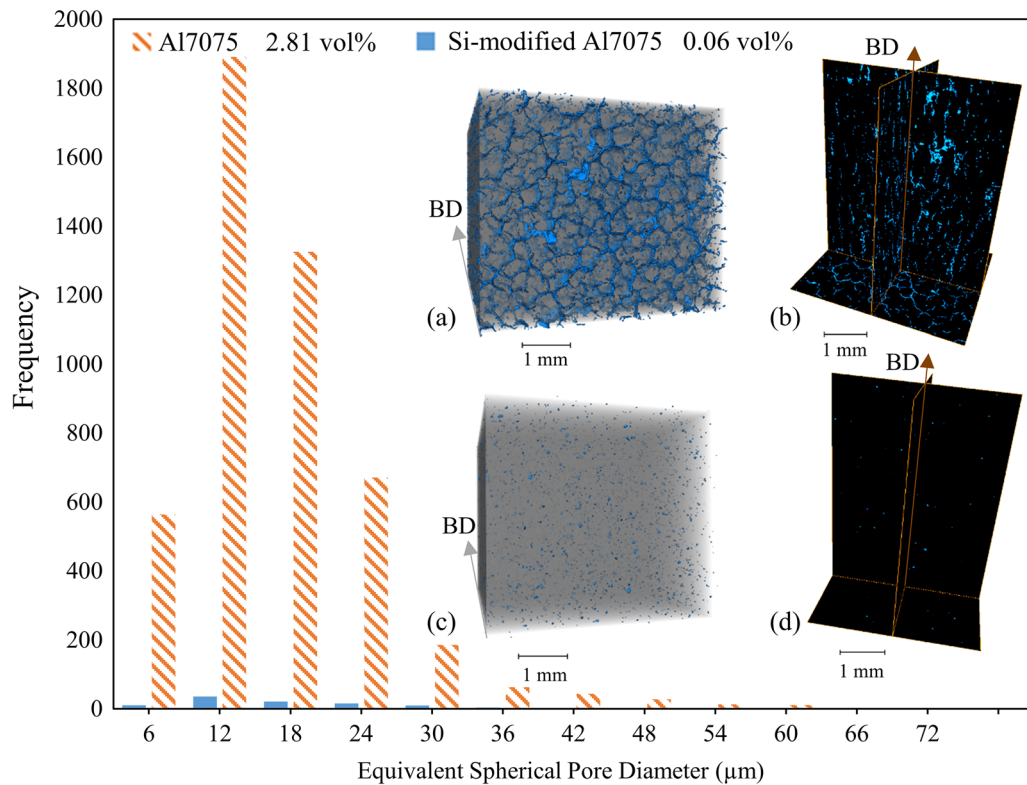


Fig. 4—Reconstructed $\mu\text{-CT}$ data showing the size and distribution of internal pores in as-built samples. The pores in the reconstructed cuboids and representative cross-sections appear as blue spots: (a, b) Al7075. (c, d) Si-modified Al7075. The building direction (BD) of the samples is indicated by the arrow.

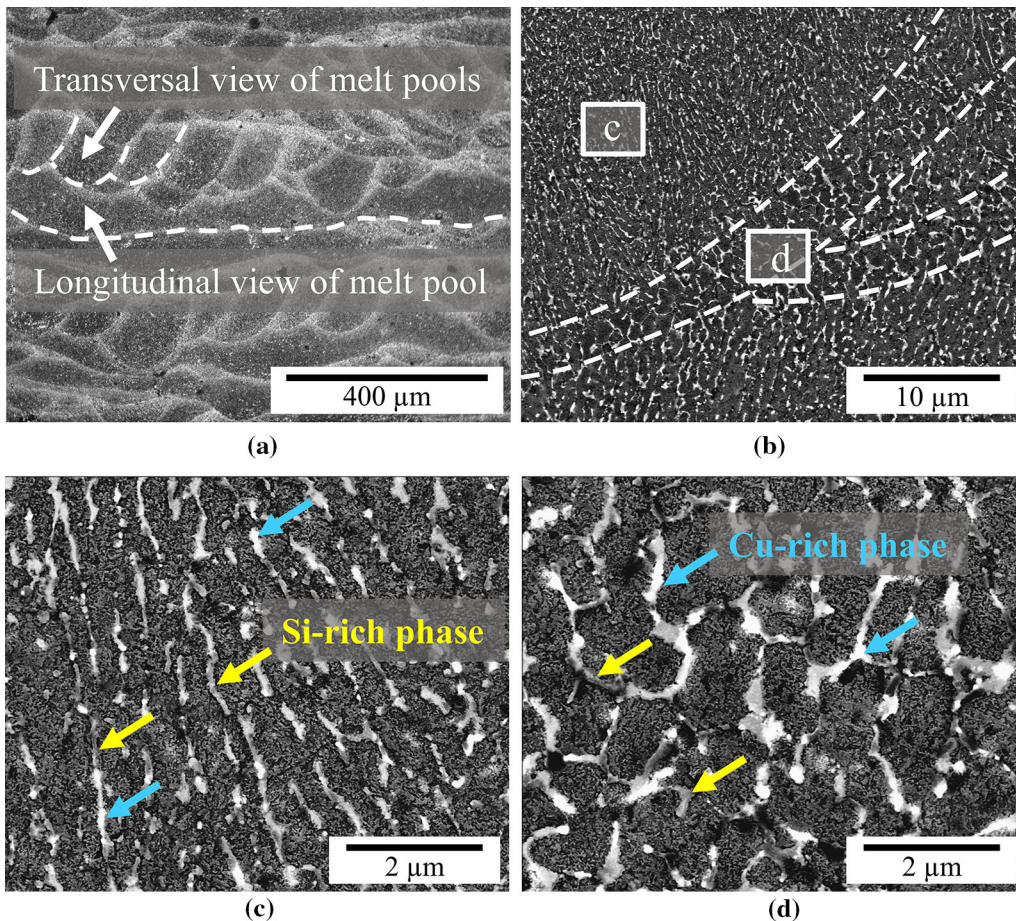


Fig. 5—(a) An etched cross-sectional OM image shows the hemispherical melt pools of the as-built Si-modified Al7075 sample. (b to d) SEM side views shows cellular microstructure of the Si-modified Al7075 alloy. Samples were fabricated using the following process parameter set: laser power of 350 W, scanning speed of 1250 mm/s and hatch spacing of 90 μm .

Al7075 alloy processed by L-PBF exhibits a fine cellular dendritic microstructure with Al sub-grains surrounded by continuous networks of Cu-enriched phase and eutectic $\alpha\text{-Al/Si}$ phase. The SEM-EDS elemental mappings in Figure 6 show the micro-segregation of Si, Cu, and Mg at the cells boundaries, while Zn is homogeneously distributed in the matrix. It indicates that the addition of Si and Mg increases the amount of eutectic phases.

3. Crystallographic texture

Figure 7 shows the EBSD crystallographic orientation maps and the corresponding $\{001\}$ pole figures recorded on cross-sections of the Al7075 alloy and the Si-modified 7075 aluminum alloy samples. A comparison is made between the Si-modified Al7075 samples fabricated using three hatch spacing of 70, 90 and 105 μm . The melt pools of the Al7075 alloy cannot be distinguished due to the epitaxial growth across several layers. It contains coarse columnar grains spanning different melt pools along the building direction, with a width and length up to 80 and 360 μm , respectively. Contrary to the coarse columnar grain structure observed in the L-PBF fabricated Al7075 alloy, epitaxial growth of grains is significantly

suppressed in the Si-modified Al7075 alloy. Figures 7(b) through (d) show that the individual melt pools are visible in all the three samples of the Si-modified Al7075 alloy, fabricated with different hatch spacing, due to the different grain morphologies at the melt pool boundaries and within the melt pools. Fine equiaxed grains with random crystallographic orientations are present at the melt pool boundaries. Columnar grains grow perpendicular to the melt pool boundary and towards the melt pool center, along the direction of the thermal gradient that is present within the melt pool. Though in some regions, epitaxial growth of grains can be observed at the melt pool centerline. As such, grains are refined and most of the columnar grains are confined within a single melt pool, resulting in a maximum length of around 140 μm . The average grain size of the Al7075 alloy is significantly reduced from $59.0 \pm 42.2 \mu\text{m}$ to $15.0 \pm 9.4 \mu\text{m}$ after the incorporation of Si using the same scan parameter set. Increasing the hatch spacing from 70 to 90 and 105 μm does not change the average grain size of the Si-modified Al7075 alloy significantly, with an average grain size of 17.8 ± 12.1 , 16.9 ± 10.1 , and $15.0 \pm 9.4 \mu\text{m}$, respectively. Additionally, a more pronounced $\langle 001 \rangle$ grain alignment along the building direction is present in the Al7075 sample. The

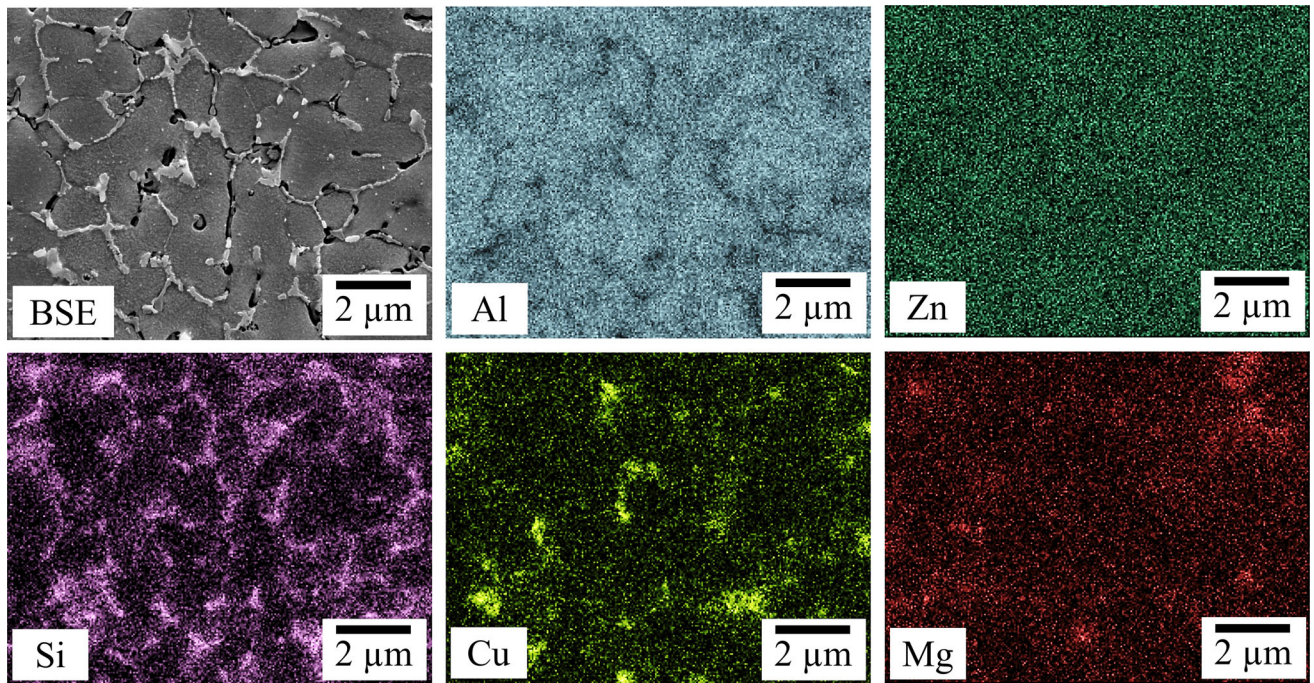


Fig. 6—SEM-EDS elemental mapping of as-built Si-modified Al7075 alloy showing the Al, Zn, Si, Cu, and Mg distribution.

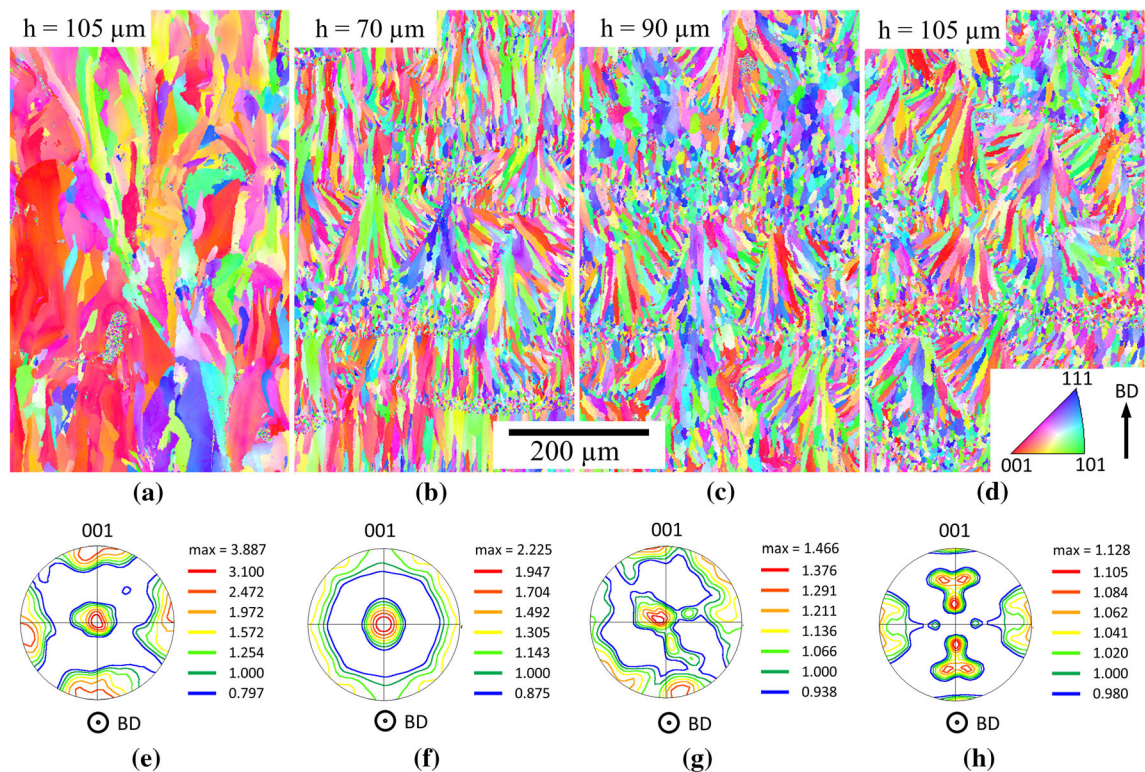


Fig. 7—(a to d) EBSD inverse pole figure (IPF) maps and (e to h) the corresponding $\{001\}$ pole figures (PFs) of (a and e) the Al7075 alloy fabricated with a hatch spacing (h) of $105\ \mu\text{m}$ and the Si-modified Al7075 alloy with different hatch spacing. (b and f) $70\ \mu\text{m}$, (c and g) $90\ \mu\text{m}$, (d and h) $105\ \mu\text{m}$. The other process parameters were fixed: power 350 W, scanning speed 1250 mm/s, layer thickness $30\ \mu\text{m}$. The IPF maps were measured on the cross-sections parallel to the building direction (BD) and the PFs were plotted with the $\{001\}$ direction parallel to the BD.

Si-modified Al7075 alloy shows a weaker $\langle 001 \rangle$ texture intensity. Furthermore, when the hatch spacing is increased from 70 to 90 and $105\ \mu\text{m}$, the $\langle 001 \rangle$ texture

continuously evolves towards more random crystallographic orientations. A texture index of 1 represents random orientations.^[39]

D. Precipitation Behavior of As-fabricated Samples During Direct Ageing

1. Vickers micro-hardness

The change in micro-hardness of the Si-modified 7075 aluminum alloy before and after direct ageing (DA) treatment at 120 °C and 150 °C as a function of holding time is presented in Figure 8. Note that direct ageing of 0 h refers to the as-fabricated condition without an ageing treatment. The two Si-modified Al7075 samples that were used for direct ageing heat treatments were fabricated with two different hatch spacing, *i.e.*, 105 μm and 90 μm , resulting in a different hardness in the as-fabricated condition, 140 ± 2 Hv and 134 ± 3 Hv, respectively. The hardness of the as-built Si-modified Al7075 sample increases with increasing holding time and reaches a peak hardness of 146 ± 3 Hv after holding for 24 h when direct aged at 120 °C, resulting in a maximum rise of 6 pct in hardness. A continuous decrease in hardness is observed by further increasing the holding time. When the DA treatment was performed at 150 °C, a similar hardness evolution is observed, while a peak hardness of 142 ± 3 Hv is obtained after a shorter holding time of 8 hours. However, in general, the Si-modified Al7075 alloy shows minimal response to precipitation hardening. The peak hardness of the Si-modified Al7075 alloy after DA is inferior to the wrought 7075 aluminum alloy under T6 condition (175 Hv).^[28]

2. XRD Phase Analysis

The XRD patterns of the as-built (AB) and direct aged (DA) samples made of the Si-modified 7075 aluminum alloy are presented in Figure 9. It reveals the presence of Al, Mg_2Si , and Si phases in both the AB and DA samples. The Cu-enriched phase which observed in the microstructure (Figure 5) is confirmed to be Al_2Cu phase. It is worth noticing that the Al_2Cu phase in the AB sample has disappeared after a DA treatment at 150 °C for 8 h. However, no other newly formed phases are detected by XRD due to the detection limit of XRD. The MgZn_2 phase, which is the main

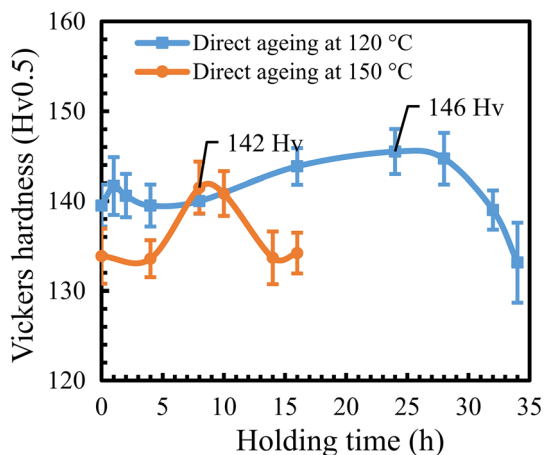


Fig. 8—Age hardening curve of the Si-modified 7075 aluminum alloy during direct ageing (DA) at 120 °C and 150 °C with different applied holding times.

strengthening phase of the 7075 aluminum alloy, is not observed. The XRD results confirm that the Al_2Cu phase forms under non-equilibrium solidification conditions, which is consistent with the thermodynamic simulation.

IV. DISCUSSION

In this part, the predictive power of the crack susceptibility index is first evaluated. Secondly, the influence of the Zn, Mg, and Si addition to the Al7075 alloy and its inhibiting effect on the formation of solidification cracks is discussed based on the solidification behavior and solidification grain structure. Finally, the influence of Zn, Mg, and Si addition on the precipitation behavior and hardness evolution during direct ageing is discussed.

A. The Inhibiting Effect of Si on the Formation of Solidification Cracks

1. Evaluation of the crack susceptibility index

As shown previously in Sections III-A and III-C, the high strength 7075 aluminum alloy is susceptible to solidification cracking during the L-PBF process, which has been widely reported by other researchers.^[11,24,40] Therefore, in alloy design, the definition of a reliable crack susceptibility index is crucial to evaluate the tendency towards cracking of alloys with modified compositions.

Alloys that are prone to solidification cracking are usually associated with a wide solidification temperature range.^[22,36] However, the L-PBF experiments show that solidification cracking was successfully mitigated after incorporating Zn, Mg, and Si in the Al7075 alloy, despite the fact that the Si-modified Al7075 alloy exhibits a more extended solidification temperature range of ~ 281 °C, as compared to the Al7075 alloy (~ 190 °C), according to the non-equilibrium simulations (Figure 2). Therefore, a more sophisticated index, Kou's model, defining the maximum steepness $\left|dT/d(f_s^{1/2})\right|$, was used to explain the absence of solidification cracks in the Si-modified Al7075 alloy.

In Kou's model, the maximum steepness $\left|dT/d(f_s^{1/2})\right|$ derived from the Temperature (T) to Fraction solid (f_s) curve near $f_s^{1/2} = 1$ was used as an index to assess the crack susceptibility. As presented in Section III-A, the additions of Zn and Mg reduced the maximum steepness $\left|dT/d(f_s^{1/2})\right|$ of the Al7075 alloy from 6504 °C to 5966 °C, indicating that a reduced crack susceptibility. Furthermore, the presence of 3.74 wt pct Si further reduced the crack susceptibility to 3960 °C.

In this model, three contributors to crack occurrence, all acting at the grain boundaries, are considered, including: (a) tensile stresses, originating from differences in volumetric shrinkage and thermal contraction, separate two neighboring dendritic columnar grains, (b) grain growth opposing the tensile separation direction, and (c) liquid feeding in the inter-dendritic region.^[31]

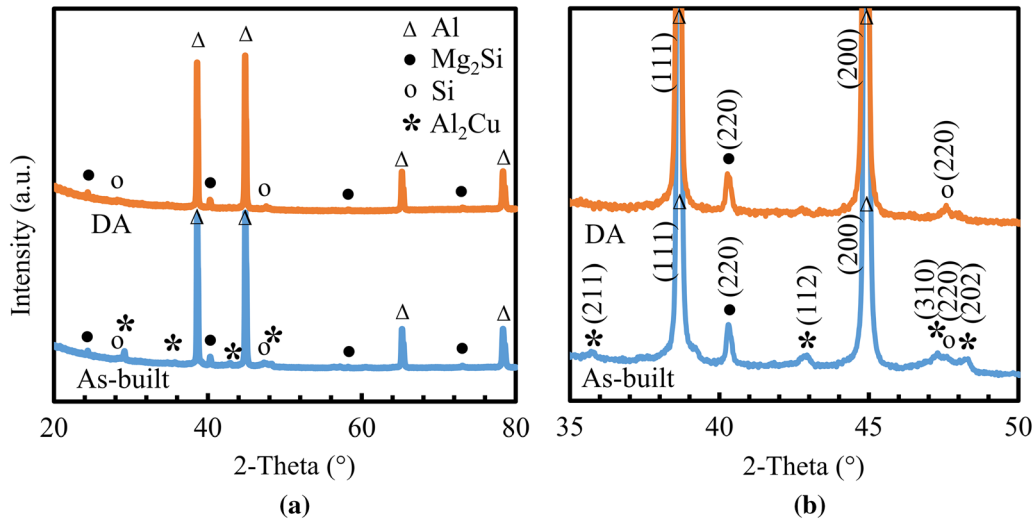


Fig. 9—X-ray diffraction patterns of the Si-modified Al7075 alloy in the as-built (AB) condition and after direct ageing (DA) at 150 °C for 8 h. (a) 2-theta range of 20 to 80 deg, (b) 2-theta range of 35 to 50 deg.

Crack formation occurs when the volume created due to the net difference between grain opening, as a result of tensile stresses, and grain closure, as a result of grain growth, exceeds the volume of liquid back feeding. In the present work, the reduced crack susceptibility induced by the incorporation of Zn, Mg, and Si in the Al7075 alloy results from the following effects. First, a smaller steepness $\left|dT/d(f_s^{1/2})\right|$ results in a faster growth rate of neighboring dendritic grains growing towards each other. The XRD and SEM micrographs in Section III-C confirmed that additional phases, including Si and Mg_2Si , were introduced and that a cellular microstructure with eutectic phases present at the cell boundaries was obtained. The increased amount of eutectic phases, including α -Al/Si and Mg_2Si phases, leads to a faster grain growth at the terminal stage of solidification, which can withstand the grain separation under tensile strain, thus exhibiting a higher crack resistance. Second, with decreased $\left|dT/d(f_s^{1/2})\right|$ steepness and increased grain growth rate, the columnar dendritic grains can better bond and shorten the length of the inter-dendritic channel. Thus the inter-dendritic liquid can flow through it easier and backfill the inter-dendritic network better. Third, a shorter inter-granular liquid channel is less favored for the crack initiation.^[31] Therefore, the addition of Zn, Mg, and Si reduced the susceptibility to cracking of Al7075 alloy during the L-PBF process.

2. Effect of Zn, Mg, and Si addition on the solidification morphology

The crack susceptibility index proposed by Kou considered the effects derived from the evolution of the solid fraction versus temperature during solidification. However, the modification of the grain morphology, especially the grain refinement effect, by adding Zn, Mg, and Si, offering additional benefits to the avoidance of solidification crack formation, was not considered. In

this section, the effects of Zn, Mg, and Si on the solidification morphology and mitigation of solidification cracking will be discussed.

As seen in Figure 4(a), a large amount of cracks were observed in the as-built Al7075 sample. The EBSD graph in Figure 7(a) shows that epitaxial growth was dominant in the Al7075 alloy resulting in coarse columnar grains that grow across different melt pools, along the building direction. During the laser melting of the Al7075 alloy, epitaxial growth occurs when the newly deposited material has the same composition and crystal structure as the previously deposited layer. The liquid metal wets the substrate completely and no undercooling is required during solidification.^[41] The newly formed grains maintain the same crystallographic orientation as the grains in the previous layer on which they nucleated. This was also facilitated by the directional heat dissipation at a high temperature gradient and minimal undercooling induced by the high thermal gradient during the L-PBF process.^[22] Thus, the melt pools cannot be distinguished based on the grain morphology. In addition, the grains of the Al7075 alloy, resulting from epitaxial growth, are coarse due to their continuous growth from the previous layers until they were confined between adjacent grains with more favorable orientation, known as competitive growth. Due to the fast cooling of the L-PBF process, the coarse columnar grains consist of several columnar/cellular dendrites with similar orientations. During solidification, grains grow faster along the easy growth direction $\langle 001 \rangle$ and are preferentially oriented parallel to the direction of the maximum temperature gradient, namely the heat dissipation direction, which is also observed in other face-centered-cubic (fcc) materials.^[15,22,36] A maximum heat extraction direction along the building direction is dominant during the L-PBF process, resulting in a strong $\langle 001 \rangle$ texture along the building direction. This is confirmed in the inverse pole figure shown in Figure 7e.

As shown in Figures 10(a) and (c), the cracks in the as-built Al7075 sample are mainly present along the grain boundaries. The cracking mechanism is illustrated in Figure 10(e). In addition to the solidification behavior discussed based on the Kou's model, other material and process related factors can influence the solidification cracking susceptibility. The high thermal expansion coefficient of the Al7075 alloy leads to a high solidification and thermal shrinkage during the solidification process.^[42] The concomitant stress development can be intensified by the high cooling rate and high temperature gradient experienced during the L-PBF process. Therefore, the oriented coarse columnar grains of the Al7075 alloy encounter a high solidification shrinkage rate and

a high thermal contraction rate during solidification and tend to be separated under the developed tensile stress field. Given that the Al7075 alloy experiences a high strain, a high strain rate and exhibits a lack of inter-dendritic liquid during solidification, it is not surprising that the solidification cracks are prevailing.^[23,24,28] Additionally, it is easy for the cracks to propagate along the long and straight grain boundaries between the coarse columnar grains.^[11] Therefore, the L-PBF processed Al7075 alloy is prone to solidification cracking.

The EBSD graphs in Figure 7 reveal a substantial difference in terms of grain morphology and size, when comparing the microstructures of the L-PBF processed

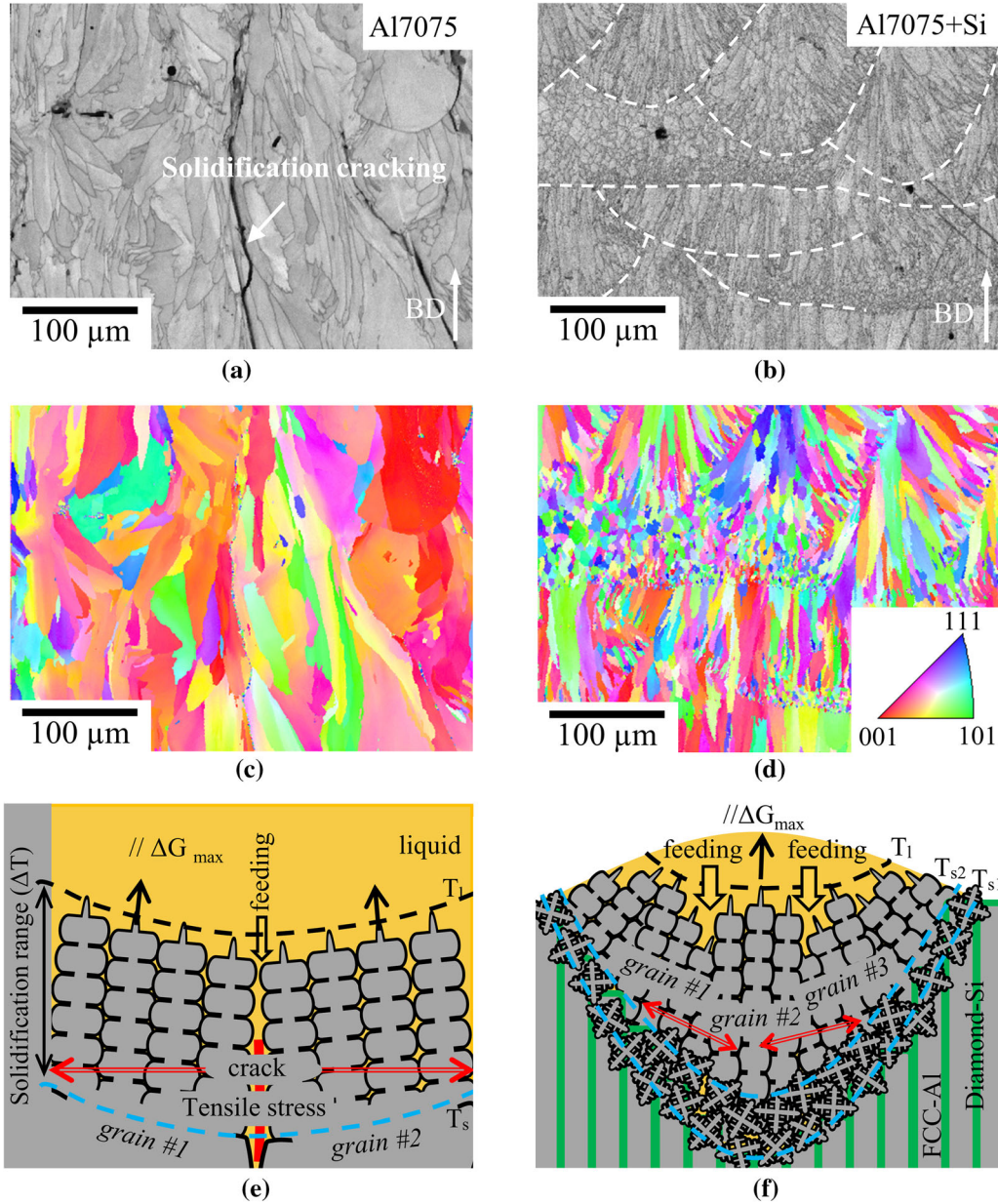


Fig. 10—Grain morphology of (a, c) L-PBF processed Al7075 with solidification cracks, and (b, d) crack-free Si-modified Al7075 alloy processed by L-PBF. Schematic of (e) epitaxial growth of the Al7075 alloy and (f) the solidification cracking mitigation mechanism in the Si-modified Al7075 alloy.

Table II. Chemical Composition (Wt Pct) of Alloys, Input Data, and Calculated Growth Restriction Factor

Alloy	Zn	Mg	Cu	Si	m_{X_i}	k_{X_i}	Q_{TOT}
Al-Zn					- 2.97	0.88	
Al-Mg					- 6.20	0.51	
Al-Cu					- 3.40	0.17	
Al-Si					- 6.60	0.11	
Al7075	4.01	1.69	1.51	0.17			11.82
Al7075 + Zn + Mg	5.10	2.67	1.55	0.17			15.30
Si-Modified Al7075	5.10	2.67	1.55	3.74			36.27

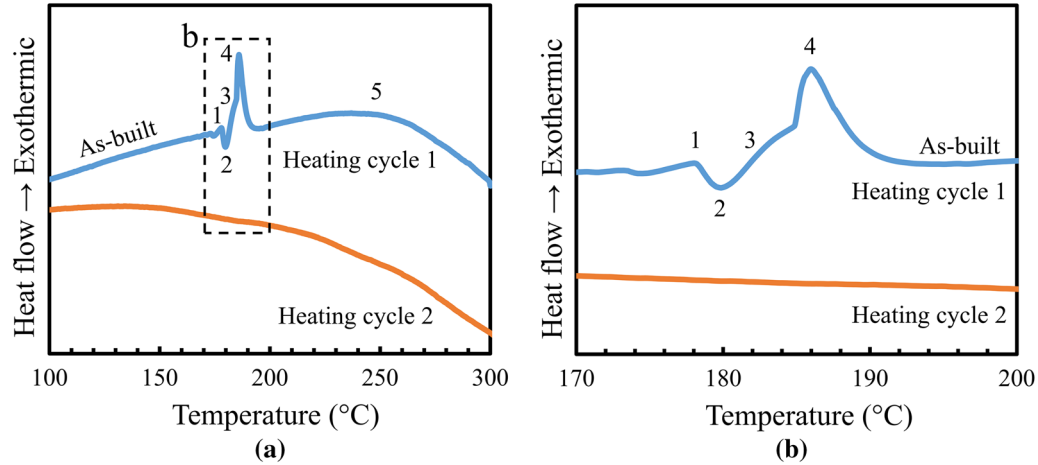


Fig. 11—DSC heating curves (heating rate 5 °C/min) of the Al-Zn-Mg-Cu-Si alloy in as-built (heating cycle 1) and as-cast (heating cycle 2) condition: (a) temperature range of 100 to 300 °C, (b) temperature range of 170 °C to 200 °C.

Al7075 alloys and Si-modified Al7075 alloy. It is observed that grains were refined and epitaxial grain growth was significantly suppressed in the Si-modified alloy. In addition, melt pools were identifiable in the Si-modified Al7075 alloy due to the presence of equiaxed grains at the melt pool boundary and columnar grains within the melt pool. The grain refinement by the addition of Zn, Mg, and Si is mainly attributed to two effects, namely grain growth restriction by eutectic forming solutes and heterogeneous nucleation on the previous deposited layer.

As observed in Figure 4, Mg, Cu, and Si segregated at the Al cell boundaries in the Si-modified Al7075 alloy due to the solute redistribution during solidification. Solute segregation at the solid/liquid front restricts the growth of grains. The grain refinement induced by solutes can be evaluated using a growth restriction parameter^[43]:

$$Q = m_{X_i}(k_{X_i} - 1)C_{X_i} \quad [2]$$

where m_{X_i} , k_{X_i} , and C_{X_i} represent the liquidus slope, equilibrium partition coefficient, and solute content of a binary Al- X_i system, respectively. The growth restriction effect in a dilute multi-components alloy system is defined as,

$$Q_{TOT} = \sum m_{X_i}(k_{X_i} - 1)C_{X_i} \quad [3]$$

It does not consider interactions among the solutes of the multi-components alloy.

The calculated growth restriction factors, induced by the different solute elements, are shown in Table II. It can be observed that the additions of Zn and Mg slightly increased the growth restriction factor from 11.82 to 15.30 for the Al7075 alloy. The restriction factor was further increased to 36.27 by the addition of Si. Therefore, the addition of solutes restricted the growth of Al grains and, thus refined the grains. Furthermore, equiaxed grains are observed at the melt pool boundary due to the heterogeneous nucleation on the previous deposited layers.^[44] As observed in Figure 7, in the melt pool center and centerline of some melt pools, competitive growth of grains was dominated, with columnar grain morphology oriented perpendicular to the melt pool boundary and towards the melt pool center. Accordingly, most of the grains were confined within the melt pools. Therefore, the grain size of the Si-modified Al7075 alloy ($16.9 \pm 10.1 \mu\text{m}$) was significantly refined compared to that of the Al7075 alloy ($59.0 \pm 42.2 \mu\text{m}$).

Moreover, increasing the hatch spacing from 70 to 105 μm contributes to more uniform crystallographic orientation resulting from a more uniform heat dissipation. Owing to the grain refinement and introduction of random oriented equiaxed grains, the increased number of grain boundaries can better accommodate the local tensile strains within a given volume. Furthermore, the presence of finer and equiaxed grains in the Si-modified Al7075 alloy can improve the liquid back-feeding ability, toughen the material, and hence make it less susceptible to crack initiation and propagation.

Overall, the mitigation of solidification cracking by the additions of Zn, Mg, and Si can be attributed to the combination of multiple contributors. First, the formation of α -Al/Si eutectic phase and Mg, Si-containing phases contributes to a higher growth rate, thus better bonding between neighboring grains. Second, the additions increase the back-feeding ability and crack initiation resistance by shortening the inter-dendritic channel length. Third, the grain refinement and introduction of equiaxed grains toughen the materials and increase the crack resistance.

In this work, the processability of the Al7075 alloy was improved by the addition of Zn, Mg, and Si to the Al7075 alloy, resulting in the manufacturing of crack-free parts with relative density values exceeding 99.94 pct by LPBF. The effects of Zn and Mg addition and Si additions on the crack susceptibility were evaluated and discussed using the maximum steepness index. The solidification cracking mitigation mechanisms were elucidated. Previously documented attempts, describing the introduction of ZrH_2 or expensive Zr/Sc modifiers to the Al7075 alloy, succeeded in eliminating solidification cracking, but an uneven distribution of the $\text{Al}_3\text{Zr}(\text{Sc})$ particles was commonly reported.^[22,24,45] The $\text{Al}_3\text{Zr}(\text{Sc})$ particles tend to segregate at the melt pool boundary and lead to an absence of primary $\text{Al}_3\text{Zr}(\text{Sc})$ particles in the melt pool center. The introduction of eutectic phases, explored in the present work, enables to obtain a more uniform distribution of relatively cheap Si throughout the whole microstructure, resulting in effective grain refinement. The current approach does not require extensive powder manipulation, including introducing ceramic particles,^[18,22,46] to modify the epitaxial growth mechanisms and refine the grains. This study provides new insights into the development of crack-free high strength Aluminum alloys for Additive Manufacturing (AM).

3. Effect of Si addition on the precipitation behavior

Direct aged Al-Zn-Mg-Cu-Si alloy samples show a minimal age-hardening response according to the micro-hardness evolution curves shown in Figure 8. Maximum rise of 6 pct in hardness was obtained after direct ageing at 150 $^\circ\text{C}$ for 8 hours. The fast cooling, inherent to the L-PBF process, led to the formation of a supersaturated FCC-Al matrix phase and the appearance of non-equilibrium phases in the solidification microstructure. The microstructure of the as-built sample, shown in Figure 5, indicates that the supersaturated FCC-Al cells are surrounded by a continuous Al/Si network and discrete Cu-rich phase particles, which

were confirmed to be Al_2Cu phase by XRD. Hadadza-deh *et al.*^[47] reported that the Mg_2Si phase also segregated along the cells' boundaries. The presence of Si, Mg_2Si , and Al_2Cu in the as-built sample was confirmed by the XRD patterns, as seen in Figure 9.

During direct ageing heat treatments at 120 $^\circ\text{C}$ and 150 $^\circ\text{C}$, the micro-hardness continuously increased and reached a peak value at 24 and 8 hours, respectively. The hardness increase was associated with the formation of precipitates. A higher heat treatment temperature enabled faster diffusion of the elements, accelerating the precipitation kinetics. The DSC heating curves, shown in Figure 11, show that multiple exothermic peaks appear between 170 $^\circ\text{C}$ and 300 $^\circ\text{C}$ in the as-built sample corresponding to the formation of several precipitates. The precipitation of metastable and stable Si, Mg_2Si , and Q (Al-Cu-Mg-Si) phases from a supersaturated Al-Si-Cu-Mg solid solution was reported upon heating.^[48–50] One endothermic peak at around 180 $^\circ\text{C}$ that was attributed to the dissolution of the Al_2Cu phase was also observed. The absence of these peaks during a second heating cycle proved that these phase transformations were driven by the supersaturation of the FCC-Al in the as-built condition. The formation of precipitates resulted in an increased hardness due to their dislocation pinning effect.

However, the increase in hardness after direct ageing heat treatment was minimal due to the limited amount of newly formed precipitates. A large amount of Si and Mg_2Si phase was already present in the as-built condition. After direct ageing, the XRD pattern did not show a significant difference except for the decomposition of the Al_2Cu phase. Additionally, Mg is more thermodynamically favorable to bind with Si rather than Zn, despite the compensation for the potential Zn and Mg losses in the starting powder. Thus, the Mg_2Si phase was formed instead of the main strengthening phase, namely MgZn_2 , of the Al7075 alloy. This proves the addition of Si changed the nature of the precipitates leading to a decreased hardness compared to Al7075-T6.^[28] Therefore, the formation of thermodynamically stable strengthening phases needs to be considered in the future Al7075 alloy development for L-PBF applications.

V. CONCLUSIONS

In this study, a gas atomized Si-modified Al7075 alloy with additions of Si, Mg, and Zn was designed to achieve crack-free and dense components by the L-PBF process. The following conclusions can be drawn:

1. Under the equilibrium solidification condition, the addition of Zn, Mg, and Si in the Al7075 alloy introduces Mg_2Si and Si phase during solidification. Additionally, Q_{AlCuMgSi} phase and V phase (Al-Zn-Cu-Mg) are formed instead of T and MgZn_2 phase. The simulation results are verified by the DSC experiments. Different from the equilibrium simulation, the non-equilibrium solidification of the Si-modified Al7075 alloy results in the formation of

Si, Q, and Al₂Cu phase. The Si and Al₂Cu phase are observed in the as-built sample manufactured by L-PBF. Moreover, the rapid solidified Si-modified Al7075 alloy processed by L-PBF exhibits a finer cellular dendritic microstructure with Al sub-grains surrounded by continuous Si and Cu-rich network as compared to the coarse dendritic microstructure obtained from the slow cooling process in a DSC.

2. According to Kou's model, the addition of Zn and Mg to the Al7075 alloy decreased the crack susceptibility $|dT/d(f_s^{1/2})|$ from 6504 °C to 5966 °C. The crack susceptibility was further decreased with increasing Si content, reaching a lowest level at the Si range of 3 to 4 wt pct. The addition of 3.74 wt pct Si results in a reduced crack susceptibility of 3960 °C.
3. Solidification cracking presented throughout the as-built Al7075 sample along the columnar grains. Solidification cracking was successfully mitigated by the additions of Zn, Mg, and Si to the Al7075 alloy. Si-modified Al7075 sample with a relative density of 99.3 ± 0.1 pct, obtained from the image analysis, and 99.94 pct, as inspected by X-ray μ -CT, was manufactured by L-PBF using the optimized laser scan parameter set: power 350 W, scanning speed 1250 mm/s, layer thickness 30 μ m, and hatch spacing 105 μ m.
4. The as-built Al7075 sample exhibited coarse columnar grains along the building direction extending across multiple layers. Epitaxial grain growth was suppressed and grains were significantly refined from 59.0 ± 42.2 μ m to 15.0 ± 9.4 μ m by the additions of Zn, Mg, and Si in the Al7075 alloy. Increasing the hatch spacing from 70 to 105 μ m, the average grain size of the Si-modified Al7075 alloy shows marginal changes; however, the crystallographic texture gradually shifted from a weak (001) texture towards more random orientations.
5. The Si-modified Al7075 alloy showed minimal age-hardening effects due to the presence of Si and Mg₂Si in the as-built sample and the decomposition of Al₂Cu phase during the subsequential ageing heat treatment. After a direct ageing heat treatment at 120 °C for 24 hours, the peak hardness of 146 ± 3 Hv was achieved by the Si-modified Al7075 alloy. Despite the increased Zn and Mg content in the starting powder, compensating for their loss during the L-PBF process, the peak hardness of the Si-modified Al7075 alloy after DA is inferior to the wrought 7075-T6 aluminum alloy (175 Hv).

ACKNOWLEDGMENTS

This work was funded by the European Union's Horizon 2020 Clean Sky 2 research and innovation program under grant agreement No 755610, project AlForAMA. The authors acknowledge the support from the topic manager, Leonardo Aircraft. L-PBF

experiments were conducted thanks to the KU Leuven funding under contract number GOA/15/012 - Sustainable Material Processing in Manufacturing. The X-ray computed tomography facilities of KU Leuven is acknowledged for the X-ray μ -CT inspections. G. Li wishes to thank the China Scholarship Council (Grant No. 201706220083) for financial support.

ELECTRONIC SUPPLEMENTARY MATERIAL

The online version of this article (<https://doi.org/10.1007/s11661-020-06073-9>) contains Supplementary material, which is available to authorized users.

REFERENCES

1. S.D. Nath, H. Irrinki, G. Gupta, M. Kearns, O. Gulsoy, and S. Atre: *Powder Technol.*, 2019, vol. 343, pp. 738–46.
2. D. Herzog, V. Seyda, E. Wycisk, and C. Emmelmann: *Acta Mater.*, 2016, vol. 117, pp. 371–92.
3. L. Xi, D. Gu, K. Lin, S. Guo, Y. Liu, Y. Li, and M. Guo: *J. Mater. Res.*, 2020, vol. 35, pp. 559–70.
4. P. Rambabu, N. Eswara Prasad, V. V. Kutumbarao, and R.J.H. Wanhill: 2017, pp. 29–52.
5. M. Zuo, M. Sokoluk, C. Cao, J. Yuan, S. Zheng, and X. Li: *Sci. Rep.*, 2019, vol. 9, pp. 1–11.
6. J. Lu, Y. Song, L. Hua, K. Zheng, and D. Dai: *J. Alloys Compd.*, 2018, vol. 767, pp. 856–69.
7. F. Bosio, A. Aversa, M. Lorusso, S. Marola, D. Gianoglio, L. Battezzati, P. Fino, D. Manfredi, and M. Lombardi: *Mater. Des.*, 2019, vol. 181, p. 107949.
8. K. Nishimoto, K. Saida, K. Kiuchi, and J. Nakayama: *Influence of Minor and Impurity Elements on Hot Cracking Susceptibility of Extra High-Purity Type 310 Stainless Steels*, 2011.
9. H. Zhao and T. Debroy: *Metall. Mater. Trans. B.*, 2001, vol. 32B, pp. 163–72.
10. G. Agarwal, A. Kumar, H. Gao, M. Amirthalingam, S.C. Moon, R.J. Dippenaar, I.M. Richardson, and M.J.M. Hermans: *Metall. Mater. Trans. A*, 2018, vol. 49A, pp. 1015–20.
11. A. Aversa, G. Marchese, A. Saboori, E. Bassini, D. Manfredi, S. Biamino, D. Ugues, P. Fino, and M. Lombardi: *Materials (Basel)*, 2019, vol. 12, p. 1007.
12. T. Boellinghaus, J.C. Lippold, and C.E.C. Editors: *Cracking Phenomena in Welds IV*. Springer, Cham, 2016.
13. G. Agarwal, A. Kumar, I.M. Richardson, and M.J.M. Hermans: *Mater. Des.*, 2019, vol. 183, p. 108104.
14. P.A. Hooper: *Addit. Manuf.*, 2018, vol. 22, pp. 548–59.
15. M.L. Montero-Sistiaga, Z. Liu, L. Bautmans, S. Nardone, G. Ji, J.-P. Kruth, J. Van Humbeeck, and K. Vanmeensel: *Addit. Manuf.*, 2020, vol. 31, p. 100995.
16. R. Mertens, S. Dadbakhsh, J. Van Humbeeck, and J.P. Kruth: *Proc. CIRP*, 2018, vol. 74, pp. 5–11.
17. D. Buchbinder, W. Meiners, N. Pirch, K. Wissenbach, and J. Schrage: *J. Laser Appl.*, 2014, vol. 26, p. 012004.
18. M. Chen, X. Li, G. Ji, Y. Wu, Z. Chen, W. Baekelant, K. Vanmeensel, H. Wang, and J.-P. Kruth: *Appl. Sci.*, 2017, vol. 7, p. 250.
19. P. Wang, C. Gammer, F. Brenne, T. Niendorf, J. Eckert, and S. Scudino: *Composites B*, 2018, vol. 147, pp. 162–68.
20. D. Carluccio, M.J. Birmingham, Y. Zhang, D.H. StJohn, K. Yang, P.A. Rometsch, X. Wu, and M.S. Dargusch: *J. Manuf. Process.*, 2018, vol. 35, pp. 715–20.
21. M. Sokoluk, C. Cao, S. Pan, and X. Li: *Nat. Commun.*, 2019, vol. 10, pp. 1–8.
22. J.H. Martin, B.D. Yahata, J.M. Hundley, J.A. Mayer, T.A. Schaedler, and T.M. Pollock: *Nature*, 2017, vol. 549, pp. 365–69.

23. L. Zhou, H. Pan, H. Hyer, S. Park, Y. Bai, B. McWilliams, K. Cho, and Y. Sohn: *Scr. Mater.*, 2019, vol. 158, pp. 24–28.
24. Z. Lei, J. Bi, Y. Chen, X. Chen, X. Qin, and Z. Tian: *Powder Technol.*, 2019, vol. 356, pp. 594–606.
25. H. Hu, M. Zhao, X. Wu, Z. Jia, R. Wang, W. Li, and Q. Liu: *J. Alloys Compd.*, 2016, vol. 681, pp. 96–108.
26. F. Sun, G.L. Nash, Q. Li, E. Liu, C. He, C. Shi, and N. Zhao: *J. Mater. Sci. Technol.*, 2017, vol. 33, pp. 1015–22.
27. G. Bo, F. Jiang, Z. Dong, G. Wang, and H. Zhang: *Mater. Sci. Eng. A*, 2019, vol. 755, pp. 147–57.
28. M.L. Montero Sistiaga, R. Mertens, B. Vrancken, X. Wang, B. Van Hooreweder, J.P. Kruth, and J. Van Humbeeck: *J. Mater. Process. Technol.*, 2016, vol. 238, pp. 437–45.
29. C. Huang, G. Cao, and S. Kou: *Sci. Technol. Weld. Join.*, 2004, vol. 9, pp. 149–57.
30. M. Rappaz, J.M. Drezet, and M. Gremaud: *Metall. Mater. Trans. A*, 1999, vol. 30A, pp. 449–55.
31. S. Kou: *Acta Mater.*, 2015, vol. 88, pp. 366–74.
32. J. Liu and S. Kou: *Acta Mater.*, 2017, vol. 125, pp. 513–23.
33. P. Schaffnit, C. Stallybrass, J. Konrad, F. Stein, and M. Weinberg: *Calphad Comput. Coupling Phase Diagrams Thermochem.*, 2015, vol. 48, pp. 184–88.
34. G.H. Gulliver: *The Quantitative Effect of Rapid Cooling upon the Constitution of Binary Alloys*, vol. 9, 1913.
35. R. Cohn, B. Fullenwider, K. Ma, and J.M. Schoenung: *Adv. Eng. Mater.*, 2018, vol. 20, pp. 1–7.
36. N.T. Aboulkhair, M. Simonelli, L. Parry, I. Ashcroft, C. Tuck, and R. Hague: *Prog. Mater. Sci.*, 2019, vol. 106, p. 100578.
37. X. Gong, T. Anderson, and K. Chou: *Manuf. Rev.*, <https://doi.org/10.1051/mfreview/2014001>.
38. S.M. Gaytan, L.E. Murr, F. Medina, E. Martinez, M.I. Lopez, and R.B. Wicker: *Mater. Technol.*, 2009, vol. 24, pp. 180–90.
39. L. Thijs, K. Kempen, J.P. Kruth, and J. Van Humbeeck: *Acta Mater.*, 2013, vol. 61, pp. 1809–19.
40. T. Böllinghaus, H. Herold, C.E. Cross, and J.C. Lippold: *Hot Cracking Phenomena in Welds II*, Springer, Berlin, 2008.
41. J.C. Lippold: *Weld. Metall. Weldability*, 2014, vol. 9781118230, pp. 1–400.
42. M. Kang and C. Kim: *J. Weld. Join.*, 2017, vol. 35, pp. 79–88.
43. A.M. Mitrašinović and F.C.R. Hernández: *Mater. Sci. Eng. A*, 2012, vol. 540, pp. 63–69.
44. Y.J. Liu, Z. Liu, Y. Jiang, G.W. Wang, Y. Yang, and L.C. Zhang: *J. Alloys Compd.*, 2018, vol. 735, pp. 1414–21.
45. L. Zhou, H. Pan, H. Hyer, S. Park, Y. Bai, B. McWilliams, K. Cho, and Y. Sohn: *Scr. Mater.*, 2019, vol. 158, pp. 24–28.
46. K.R. Ramkumar, H. Bekele, and S. Sivasankaran: *Adv. Mater. Sci. Eng.*, 2015, vol. 2015, pp. 1–14.
47. A. Hadadzadeh, B.S. Amirkhiz, and M. Mohammadi: *Mater. Sci. Eng. A*, 2019, vol. 739, pp. 295–300.
48. E. Sjölander and S. Seifeddine: *Metall. Mater. Trans. A*, 2014, vol. 45A, pp. 1916–27.
49. A.M. Samuel, J. Gauthier, and F.H. Samuel: *Metall. Mater. Trans. A*, 1996, vol. 27A, pp. 1785–98.
50. V.C. Pierre, B. Anthony, T. Lore, V.H. Brecht *et al.*: *Congr. Exhib.*, 2018, vol. 2020, pp. 1–7.

Publisher's Note Springer Nature remains neutral with regard to jurisdictional claims in published maps and institutional affiliations.